Supporting Information

Non-Pinned and Reversible Spin Crossover in Self-Assembled Monolayers of a Functionalised Fe(II) Scorpionate Complex

Rebecca Rodrigues de Miranda, Niccolò Giaconi, Margaux Pénicaud, Lisa Biwandu, Thierry Buffeteau, Gilles Pécastaings, Brunetto Cortigiani, Matteo Mannini, Edwige Otero, Philippe Ohresser, Elizabeth A. Hillard, Lorenzo Poggini,* Mathieu Gonidec,* Patrick Rosa**

Table of contents

Figure S1. Magnetometry 2
Figure S2. Atomic Force Microscopy (AFM) imaging 4
Figure S3a. Time of Flight Secondary Ion Mass Spectrometry (ToF-SIMS) 5
Figure S3b. Time of Flight Secondary Ion Mass Spectrometry (ToF-SIMS) 7
Figure S3c. Time of Flight Secondary Ion Mass Spectrometry (ToF-SIMS) 8
Figure S3d. Time of Flight Secondary Ion Mass Spectrometry (ToF-SIMS) 9
Figure S3e. Time of Flight Secondary Ion Mass Spectrometry (ToF-SIMS) 10
Figure S3f. Time of Flight Secondary Ion Mass Spectrometry (ToF-SIMS) 11
Table S1. Time of Flight Secondary Ion Mass Spectrometry (ToF-SIMS) 12
Figure S4. X-ray Photoelectron Spectroscopy (XPS) 13
Table S2. XPS semi-quantitative analysis 13
Figure S5a. Polarization-Modulated InfraRed Reflective Absorption Spectroscopy (PM-IRRAS) 14
Figure S5b. Polarization-Modulated InfraRed Reflective Absorption Spectroscopy (PM-IRRAS) 15
Figure S5c. Polarization-Modulated InfraRed Reflective Absorption Spectroscopy (PM-IRRAS) 15
Figure S5d. Polarization-Modulated InfraRed Reflective Absorption Spectroscopy (PM-IRRAS) 16
Figure S6. Electrochemistry 17
Figure S7. Geometry optimization 18
Figure S8a. Variable-temperature XPS 19
Figure S8b. Variable-temperature XPS 19
Figure S9a. X-ray Absorption Spectroscopy (XAS) 21
Figure S9b. X-ray Absorption Spectroscopy (XAS) 22
Figure S9c. X-ray Absorption Spectroscopy (XAS) 23
Figure S9d. X-ray Absorption Spectroscopy (XAS) 24
Figure S9e. X-ray Absorption Spectroscopy (XAS) 25
Figure S10. ^{1}H NMR monitoring of stability in solution 26

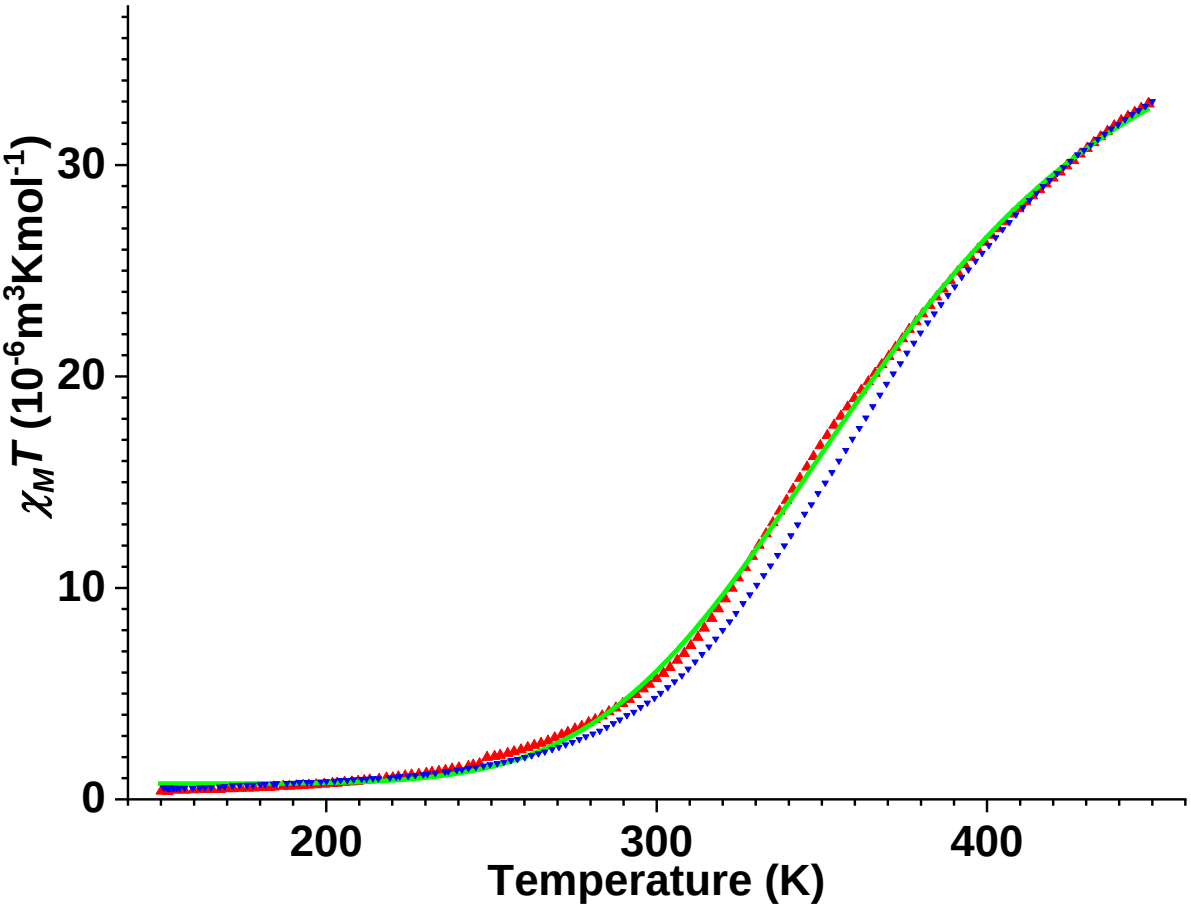

Figure S1. Magnetometry

Vibrating Sample Magnetometer (VSM) magnetic measurement on bulk $\mathbf{M_{SAc}}$, in the warming mode (red triangles) and in the cooling mode (blue triangles). The green curve represents the Boltzmann equilibrium fitting of the warming mode.

The raw magnetic data was converted to the molar susceptibility product with temperature, $\chi_M T$, after removing the sample holder magnetic background and sample diamagnetic contribution, estimated using Pascal's constants.

Below 200 K, $\chi_M T$ is very close to zero at 5×10^{-7} m^3 K mol^{-1}, in agreement with an essentially diamagnetic state. $\chi_M T$ increases monotonically with temperature above 250 K, to reach 33.0×10^{-6} m^3 K mol^{-1} at 450 K. This value is lower than the spin-only value of 37.7×10^{-6} m^3 K mol^{-1} expected for a HS Fe(II) complex with S = 2 and a g value of 2.0, but as can be seen the crossover is not complete at this temperature. A change in the curve slope is observed around 335 K, indicating some change in the complex, which we link to its melting within the sample holder. The compound was indeed found to start melting above 68°C independently. Accordingly, the measurement in the cooling mode does not fully follow the curve. Subsequent measurements stay close to both curves. We fitted the warming mode measurement considering the Boltzmann equilibrium between the two states described by Eq.1:

$$\chi_M T = \frac{\chi_M T_{max}}{1+exp\left(\frac{\Delta H}{RT}+\frac{\Delta S}{R}\right)} + residue \qquad \text{Eq. 1}$$

We obtained a satisfying fit (R^2 of 0.99949) with a value of 39.1(1)×10^{-6} m^3 K mol^{-1} for $\chi_M T_{max}$, a value slightly above the spin-only value for HS Fe(II). ΔH and ΔS values of 25.1(1) kJ mol^{-1} and 68.4(3) J K^{-1} mol^{-1} are in agreement with a non-cooperative SCO with $T_{1/2} = {\Delta H}/{\Delta S} = 367$ K . The residue of 7.4(1) ×10^{-7} m^3 K mol^{-1} shows an almost complete SCO to the diamagnetic state. We used the value of $\chi_M T_{max}$ obtained by the fit to calculate the HS fraction n_{HS} reported in the main text in Figure 5.

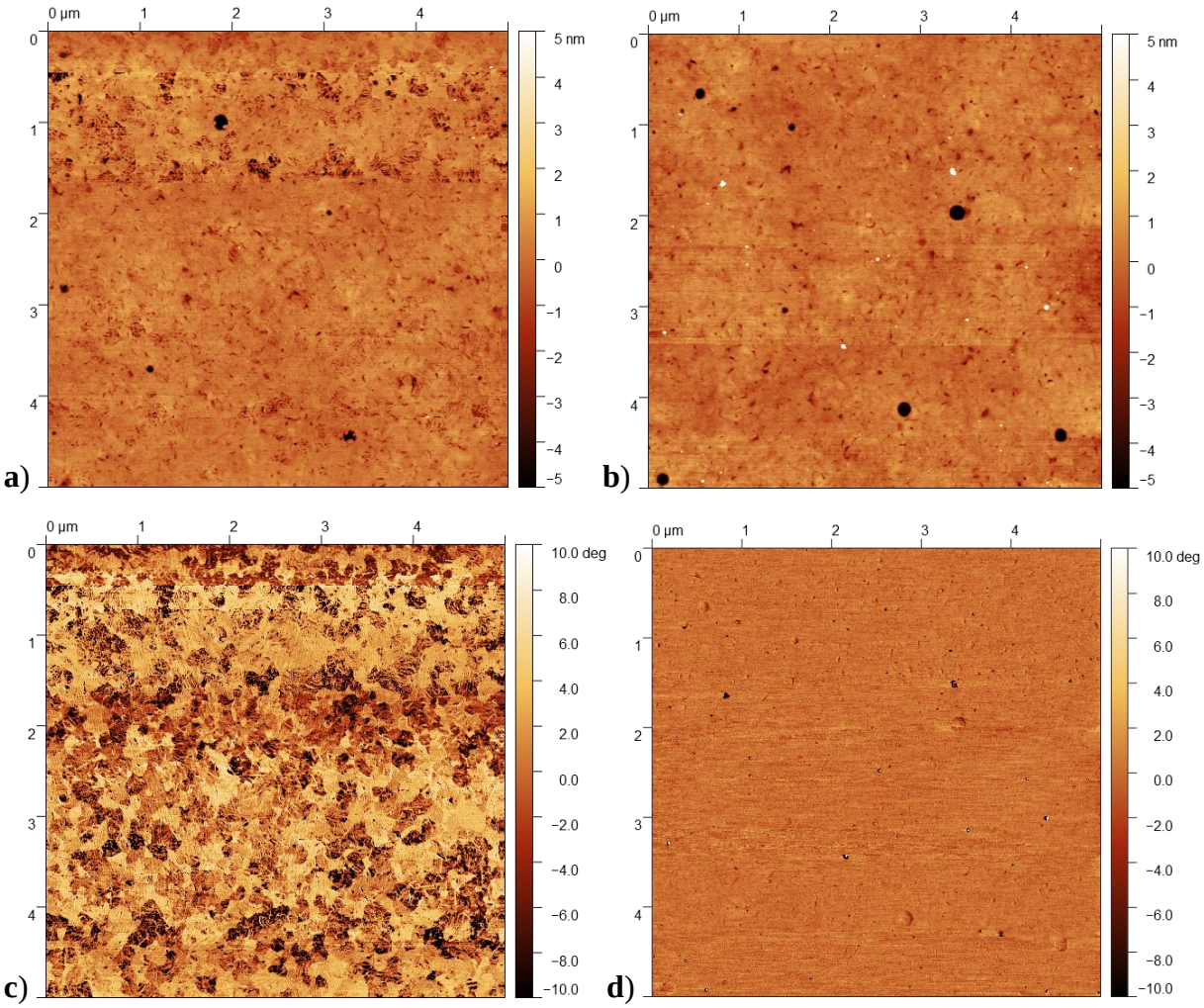

Figure S2. Atomic Force Microscopy (AFM) imaging

AFM height maps of a bare template stripped gold substrate (**a**, top left) and of a SAM of **M$_{SAu}$** on template stripped gold (**b**, top right), on a 5 × 5 µm area. The SAM is uniform and marginally rougher than the bare gold, with a RMS roughness of 7.1 Å compared to 6.9 Å for the substrate. The corresponding phase images are clearly distinct for the bare substrate (**c**, bottom left) and the SAM (**d**, bottom right).

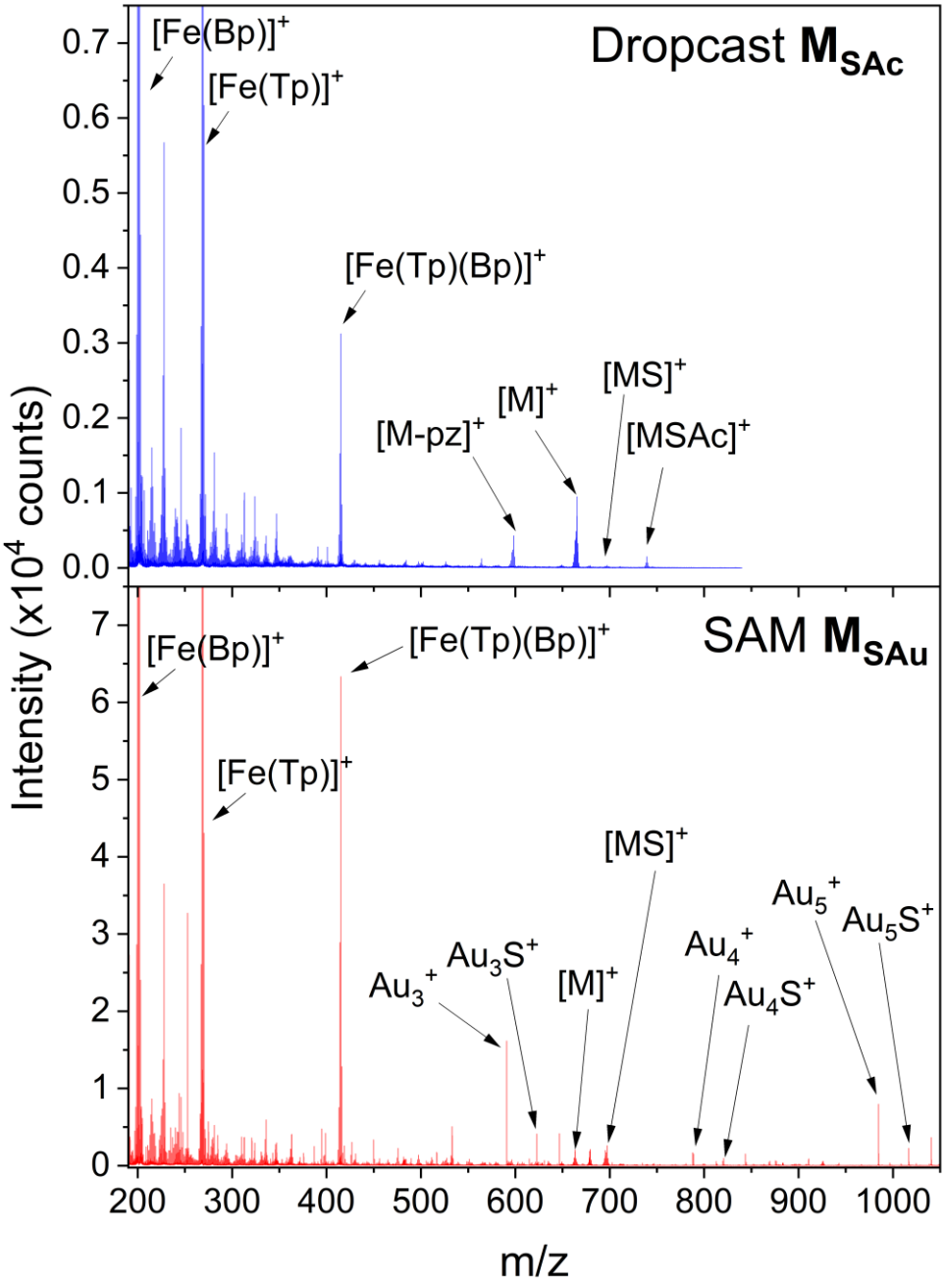

Figure S3a. Time of Flight Secondary Ion Mass Spectrometry (ToF-SIMS)

Positive ToF-SIMS spectra on a 500 × 500 µm area of (top) a bulk sample (dropcast of a methanol solution) of $\mathbf{M_{SAc}}$; (bottom) a $\mathbf{M_{SAu}}$ SAM.

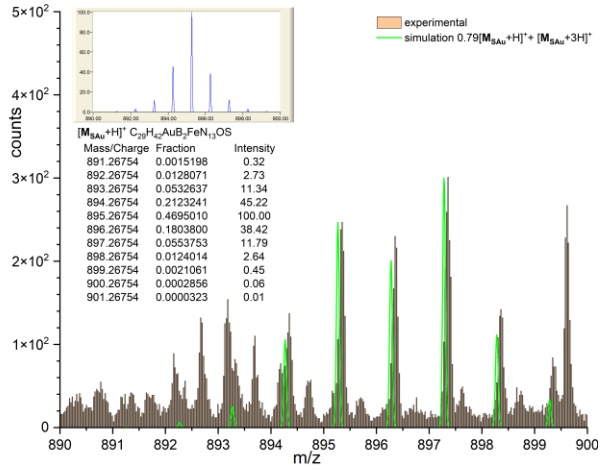

$[M_{SAu}+H]^+$ $C_{29}H_{42}AuB_2FeN_{13}OS$

Mass/Charge	Fraction	Intensity
891.26754	0.0015198	0.32
892.26754	0.0128071	2.73
893.26754	0.0532637	11.34
894.26754	0.2123241	45.22
895.26754	0.4695010	100.00
896.26754	0.1803800	38.42
897.26754	0.0553753	11.79
898.26754	0.0124014	2.64
899.26754	0.0021061	0.45
900.26754	0.0002856	0.06
901.26754	0.0000323	0.01

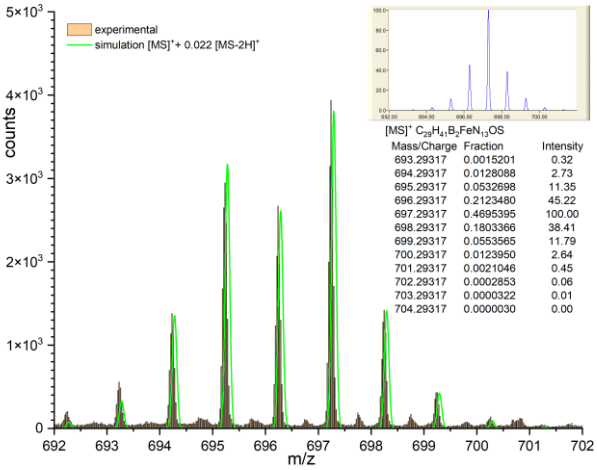

$[MS]^+$ $C_{29}H_{41}B_2FeN_{13}OS$

Mass/Charge	Fraction	Intensity
693.29317	0.0015201	0.32
694.29317	0.0128088	2.73
695.29317	0.0532698	11.35
696.29317	0.2123480	45.22
697.29317	0.4695395	100.00
698.29317	0.1803366	38.41
699.29317	0.0553565	11.79
700.29317	0.0123950	2.64
701.29317	0.0021046	0.45
702.29317	0.0002853	0.06
703.29317	0.0000322	0.01
704.29317	0.0000030	0.00

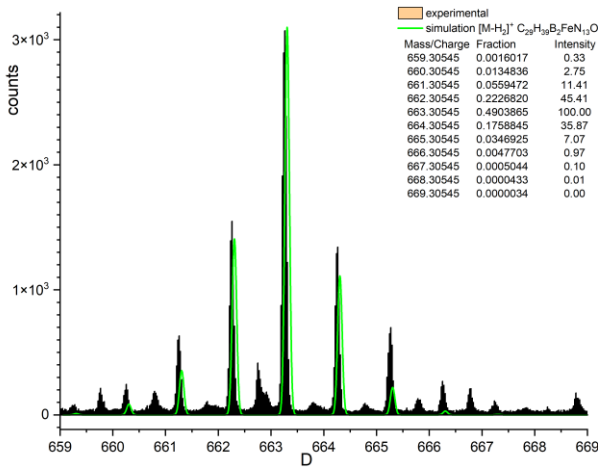

Mass/Charge	Fraction	Intensity
659.30545	0.0016017	0.33
660.30545	0.0134836	2.75
661.30545	0.0559472	11.41
662.30545	0.2226820	45.41
663.30545	0.4903865	100.00
664.30545	0.1758845	35.87
665.30545	0.0346925	7.07
666.30545	0.0047703	0.97
667.30545	0.0005044	0.10
668.30545	0.0000433	0.01
669.30545	0.0000034	0.00

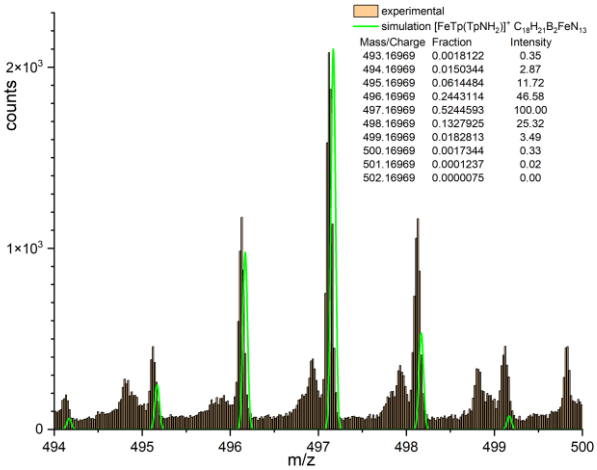

Mass/Charge	Fraction	Intensity
493.16969	0.0018122	0.35
494.16969	0.0150344	2.87
495.16969	0.0614484	11.72
496.16969	0.2443114	46.58
497.16969	0.5244593	100.00
498.16969	0.1327925	25.32
499.16969	0.0182813	3.49
500.16969	0.0017344	0.33
501.16969	0.0001237	0.02
502.16969	0.0000075	0.00

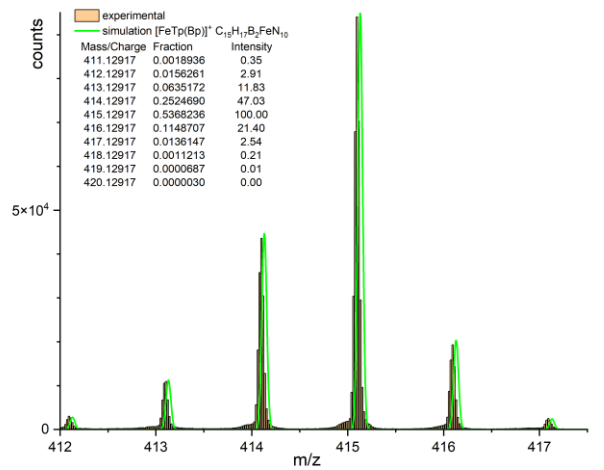

Mass/Charge	Fraction	Intensity
411.12917	0.0018936	0.35
412.12917	0.0156261	2.91
413.12917	0.0635172	11.83
414.12917	0.2524690	47.03
415.12917	0.5368236	100.00
416.12917	0.1148707	21.40
417.12917	0.0136147	2.54
418.12917	0.0011213	0.21
419.12917	0.0000687	0.01
420.12917	0.0000030	0.00

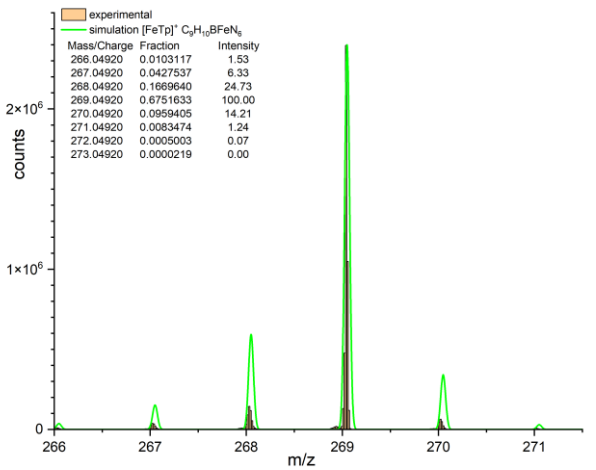

Mass/Charge	Fraction	Intensity
266.04920	0.0103117	1.53
267.04920	0.0427537	6.33
268.04920	0.1669640	24.73
269.04920	0.6751633	100.00
270.04920	0.0959405	14.21
271.04920	0.0083474	1.24
272.04920	0.0005003	0.07
273.04920	0.0000219	0.00

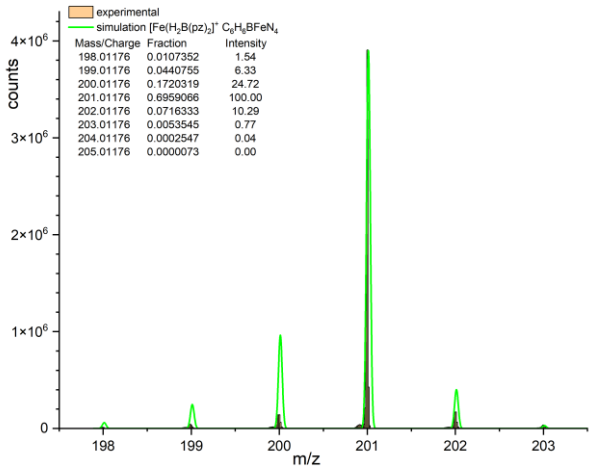

Figure S3b. Time of Flight Secondary Ion Mass Spectrometry (ToF-SIMS)

ToF-SIMS positive spectra of a **M**$_{\mathbf{SAu}}$ SAM on a 500 × 500 µm area. Experimental data (black histograms) and calculated isotopic distributions (green curves) corresponding to the grafted molecule [**M**$_{\mathbf{SAu}}$]$^+$ (mixture of protonated clusters), the molecular peak [**M**$_{\mathbf{S}}$]$^+$, as well as the five most abundant peaks originating from molecular fragmentation during measurement: [**M**-H_2]$^+$ (loss of S and H_2), [FeTp(TpNH$_2$)]$^+$ (loss of the spacer chain), [FeTpBp]$^+$ (loss of functionalized pyrazole), [FeTp]$^+$ (loss of functionalized Tp), [FeBp$_2$]$^+$ (loss of functionalized pyrazole plus another pyrazole).

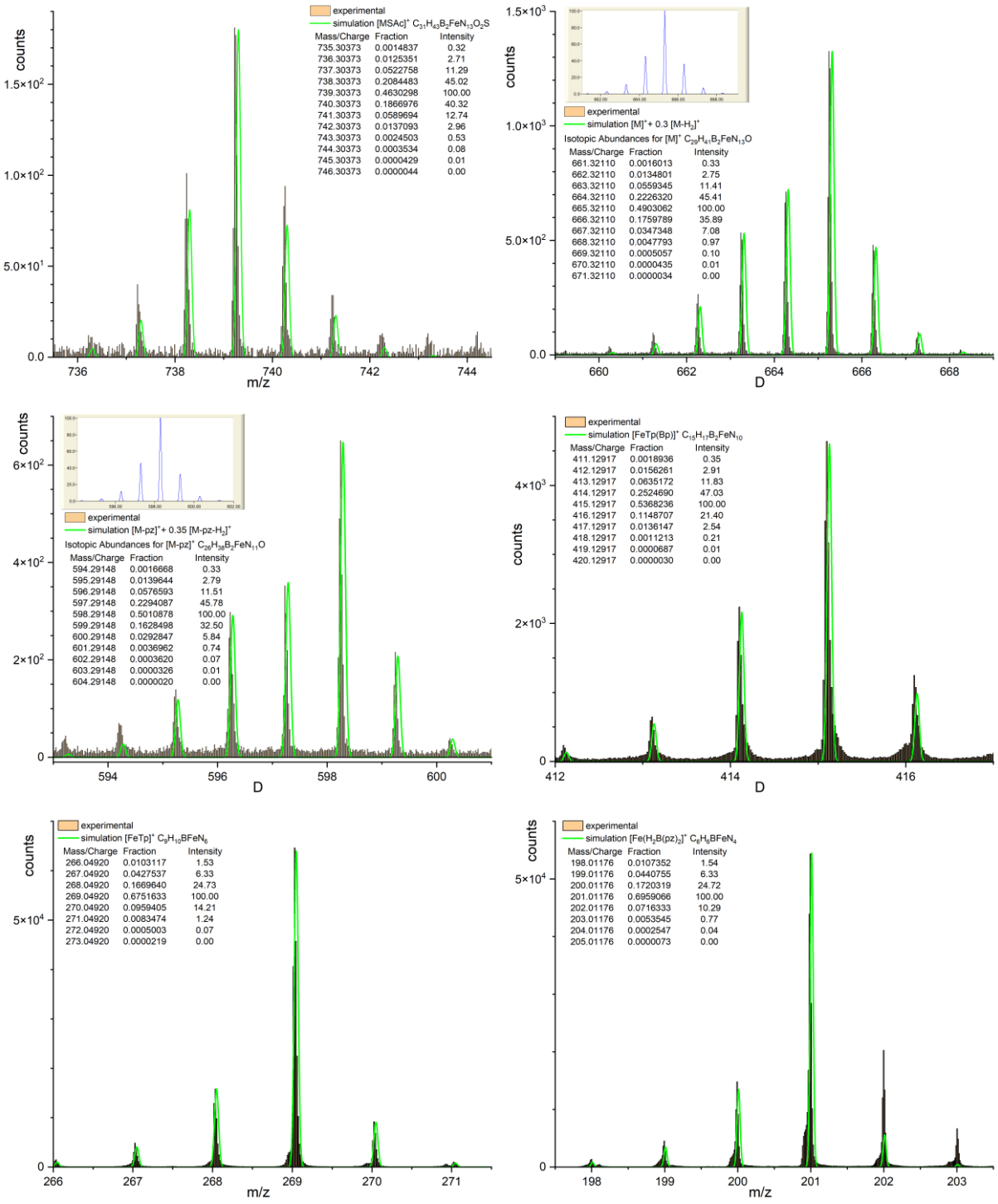

Figure S3c. Time of Flight Secondary Ion Mass Spectrometry (ToF-SIMS)

ToF-SIMS positive spectra of the dropcast of a methanol solution of $\mathbf{M_{SAc}}$ on a 500 × 500 µm area. Experimental data (black histograms) and calculated isotopic distributions (green curves) corresponding to the molecule $[\mathbf{M_{SAc}}]^+$, as well as the five most abundant molecular peaks originating from molecular fragmentation during measurement. While $[\mathbf{M}\text{-}H_2]^+$, $[FeTpBp]^+$, $[FeTp]^+$ and $[FeBp_2]^+$ were observed as in the case of the grafted molecule (Figure S3b), we observe $[\mathbf{M}\text{-}pz]^+$ (loss of an unfunctionalized pyrazole) and no $[FeTp(TpNH_2)]^+$ for the dropcast molecule.

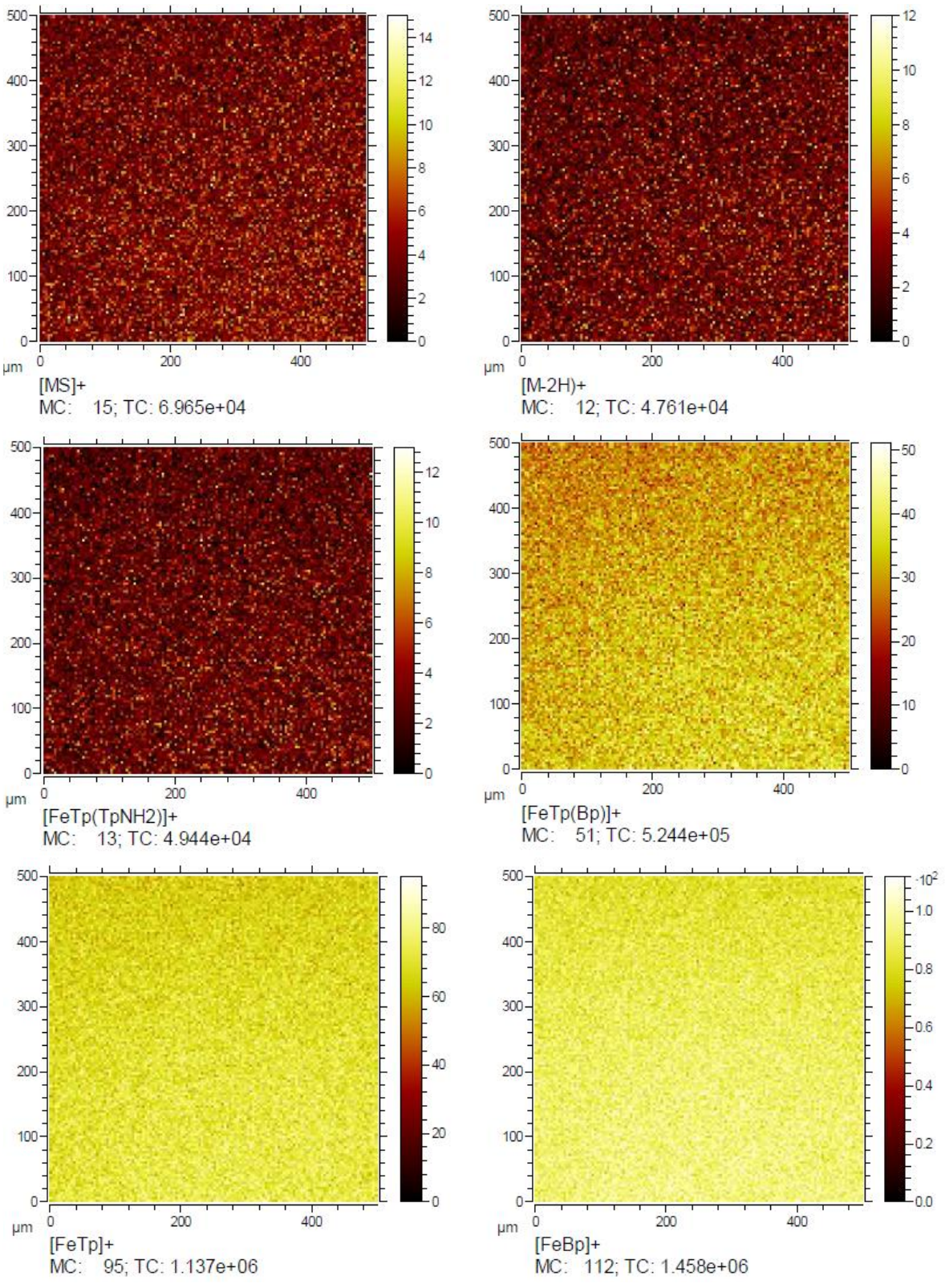

Figure S3d. Time of Flight Secondary Ion Mass Spectrometry (ToF-SIMS)

ToF-SIMS secondary ion mapping of an **M$_{SAu}$** SAM on a 500 × 500 µm area. The molecule and its fragments are homogeneously distributed over the imaged area.

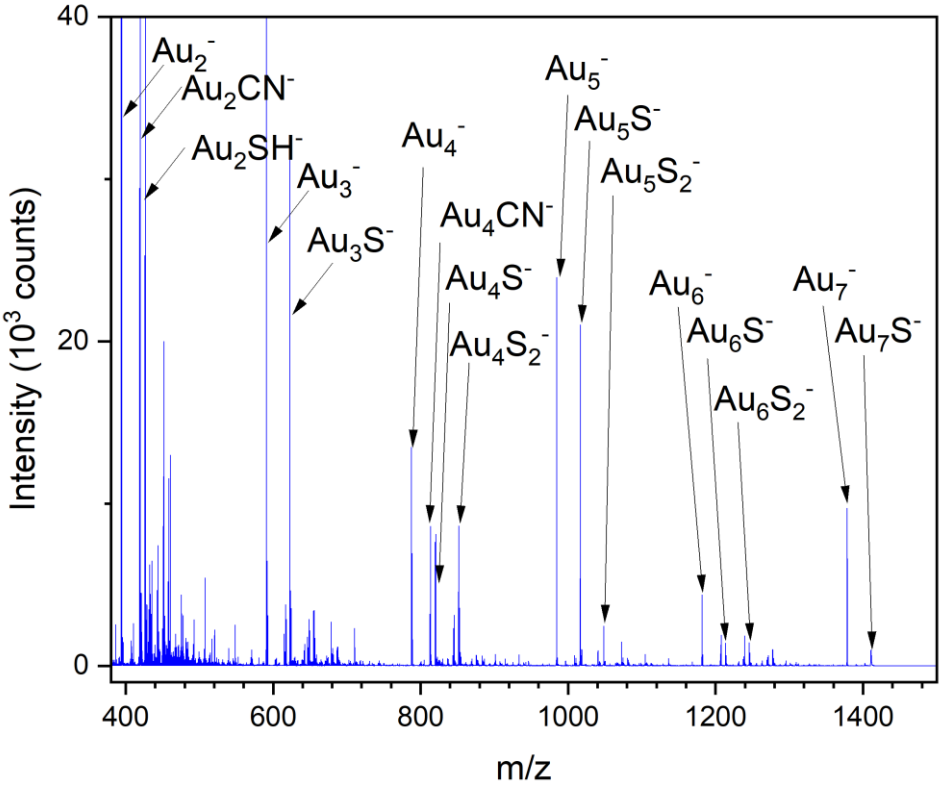

Figure S3e. Time of Flight Secondary Ion Mass Spectrometry (ToF-SIMS)

ToF-SIMS spectrum of a $\mathbf{M_{SAu}}$ SAM on Au^{TS} on a 500 × 500 µm area in negative mode.

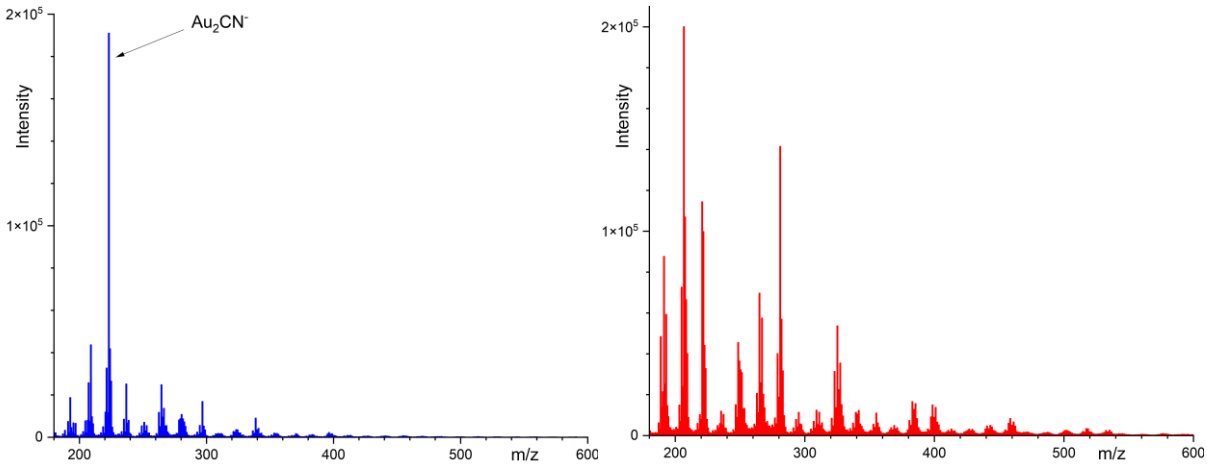

Figure S3f. Time of Flight Secondary Ion Mass Spectrometry (ToF-SIMS)

ToF-SIMS spectra of a pristine Au^{TS} substrate in the negative mode (left, in blue) and positive mode (right, in red).

Fragment name	Formulas		Calculated m/z (main peak)	SAM (main peak)	Dropcast (main peak)
$[Fe(Bp)]^+$	$[Fe(H_2B(pz)_2]^+$	$C_6H_6BFeN_4$	201.012	201.002	200.994
$[Fe(Tp)]^+$	$[Fe(HB(pz)_3]^+$	$C_9H_{10}BFeN_6$	269.049	269.041	269.031
$[Fe(Tp)(Bp)]^+$	$[Fe(HB(pz)_3(H_2B(pz)_2]^+$	$C_{15}H_{17}B_2FeN_{10}$	415.129	415.097	415.100
$[Fe(Tp)(TpNH2)]^+$	$[Fe(HB(pz)_3(HB(pz)_2(pzNH_2)]^+$	$C_{18}H_{21}B_2FeN_{13}$	497.170	497.121	
Au_3		Au_3	590.900	590.823	
Au_3S		Au_3S	622.872	622.806	
$[\mathbf{M}\text{-pz-2H}]^+$	$[Fe(HB(pz)_3(HB(pz)(pzNHCOC_{10}H_{19})]^+$	$C_{26}H_{36}B_2FeN_{11}O$	596.276		596.233
$[\mathbf{M}\text{-pz}]^+$	$[Fe(HB(pz)_3(HB(pz)(pzNHCOC_{10}H_{21})]^+$	$C_{26}H_{38}B_2FeN_{11}O$	598.291		598.249
$[\mathbf{M}\text{-2H}]^+$	$[Fe(HB(pz)_3(HB(pz)_2(pzNHCOC_{10}H_{19})]^+$	$C_{29}H_{39}B_2FeN_{13}O$	663.305	663.264	663.241
$[\mathbf{M}]^+$	$[Fe(HB(pz)_3(HB(pz)_2(pzNHCOC_{10}H_{21})]^+$	$C_{29}H_{41}B_2FeN_{13}O$	665.321		665.249
$[\mathbf{M_S}\text{-2H}]^+$	$[Fe(HB(pz)_3(HB(pz)_2(pzNHCOC_{10}H_{18}S)]^+$	$C_{29}H_{39}B_2FeN_{13}OS$	695.278	695.238	
$[\mathbf{M_S}]^+$	$[Fe(HB(pz)_3(HB(pz)_2(pzNHCOC_{10}H_{20}S)]^+$	$C_{29}H_{41}B_2FeN_{13}OS$	697.293	697.245	697.221
$[\mathbf{M_{SAc}}]^+$	$[Fe(HB(pz)_3(HB(pz)_2(pzNHCOC_{10}H_{20}SCOMe)]^+$	$C_{31}H_{43}B_2FeN_{13}O_2S$	739.304	739.251	739.226
$[\mathbf{M_{SAu}}+H]^+$	$[Fe(HB(pz)_3(HB(pz)_2(pzNHCOC_{10}H_{20}SAuH)]^+$	$C_{29}H_{42}AuB_2FeN_{13}OS$	895.268	895.352	
$[\mathbf{M_{SAu}}+3H]^+$	$[Fe(HB(pz)_3(HB(pz)_2(pzNHCOC_{10}H_{20}SAuH_3)]^+$	$C_{29}H_{44}AuB_2FeN_{13}OS$	897.283	897.360	
Au_4		Au_4	787.866	787.767	
Au_4S		Au_4S	819.838	819.723	
Au_5		Au_5	984.833	984.698	
Au_5S		Au_5S	1016.805	1016.658	
Au_5S_2		Au_5S_2	1048.777	1048.628	
Au_6		Au_6	1181.799	1181.612	
Au_6S		Au_6S	1213.771	1213.592	
Au_6S_2		Au_6S_2	1245.743	1245.524	

Table S1. Time of Flight Secondary Ion Mass Spectrometry (ToF-SIMS)

List of fragments, their formulas and calculated m/z, and the peaks observed in the SAM and dropcast ToF-SIMS spectra (positive mode). Fragments observed in both spectra are highlighted.

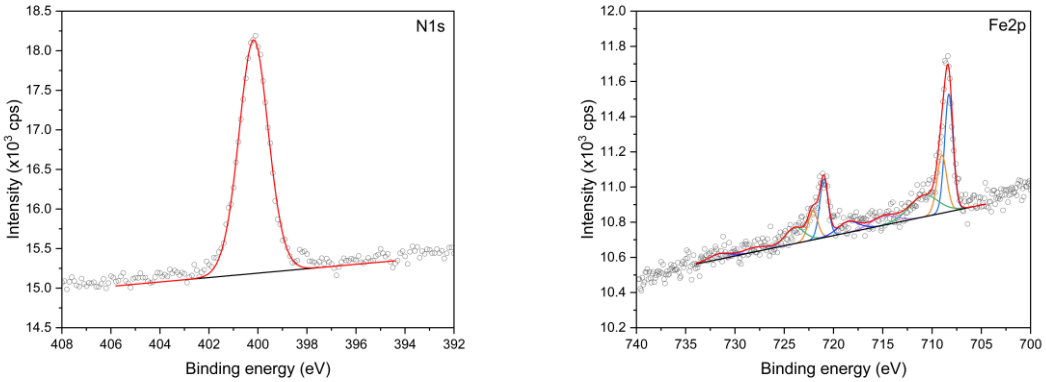

Figure S4. X-ray Photoelectron Spectroscopy (XPS)

Room temperature XPS on an **M$_{SAu}$** SAM on gold, in the N*1s* and Fe*2p* regions. The measured data is plotted as open circles, with the solid red lines corresponding to the envelopes of the fitted components. In the case of iron, the individual fitted components are represented with orange, blue and green solid lines. The spectra were fit in CasaXPS after calibrating to the *4f* peaks of the gold substrate and fitting a linear background. Calculated cross sections[1] were used and the peaks were fit with 70/30 Voigt functions.

	% composition in SAM	**% composition in bulk**	**% composition theoretical**
S	9.9 ± 0.5	7.1 ± 0.4	6.7
N	81.6 ± 4.1	88.0 ± 4.4	86.7
Fe	8.6 ± 0.4	4.9 ± 0.3	6.7

Table S2. XPS semi-quantitative analysis

Semi-quantitative analysis yields elemental ratios of Fe, N, and S that correspond to the theoretical composition, considering the small quantity of molecules in the sample and the experimental error of the XPS.

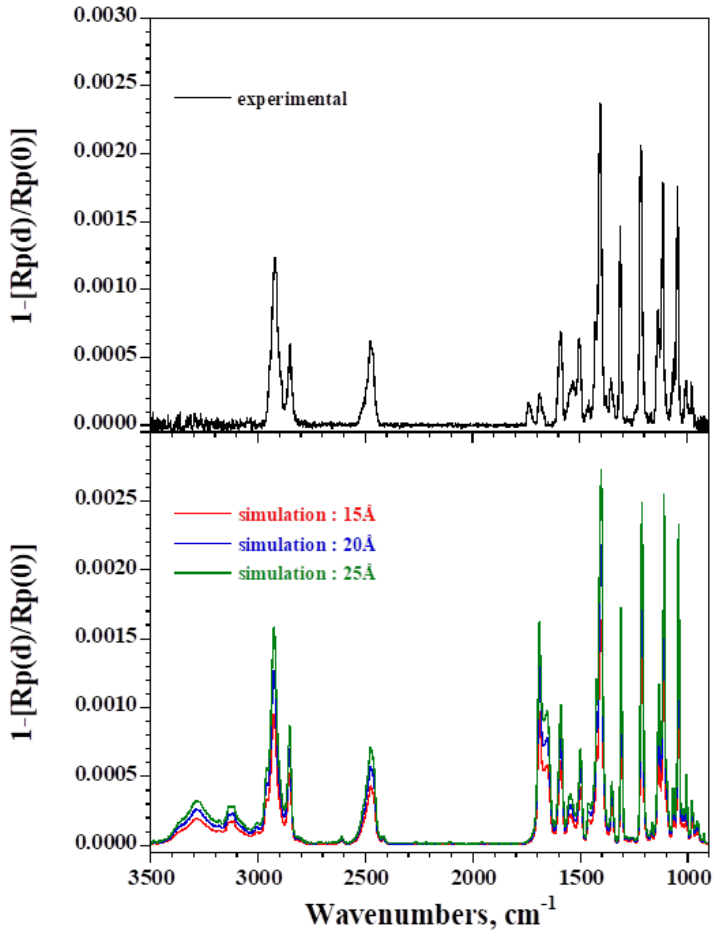

Figure S5a. Polarization-Modulated InfraRed Reflective Absorption Spectroscopy (PM-IRRAS)

Comparison of experimental IRRAS spectrum (in black) of an **M**$_{SAu}$ SAM on template stripped gold and simulated IRRAS spectra for **M**$_{SAc}$ layers of various thicknesses (15 Å in red, 20 Å in blue and 25 Å in green).

The isotropic and anisotropic optical constants (refractive index $n(\bar{\nu})$ and extinction coefficient $k(\bar{\nu})$) of **M**$_{SAc}$ have been determined from polarized ATR spectra (shown in **Figure S5b**), using the procedure described by Dignam *et. al.*.[2] Isotropic optical constants (*i.e.* similar values of the in-plane and out-of-plane refractive indexes and extinction coefficients) have been measured for **M**$_{SAc}$ (**Figures S5c and S5d**). We have checked that the intensities of the bands for this compound in the p-polarized ATR spectrum are double those measured in the s-polarized ATR spectrum, as expected for an isotropic layer. The refractive index in the visible was set to 1.5 for **M**$_{SAc}$.

The program used to calculate the IRRAS spectra for a compact monolayer of **M**$_{SAc}$ deposited onto a gold substrate is based on the Abeles' matrix formalism,[3,4] which has been generalized for anisotropic layers.[5] Several parameters must be fixed in the program, such as the thickness of the monolayer, the angle of incidence (set to 75°) and the polarization of the infrared beam. The p-polarized reflectance of the covered $R_p(d)$ and bare $R_p(0)$ substrates have been calculated using the spectral dependence of the optical constants of **M**$_{SAc}$ and of gold.[6]

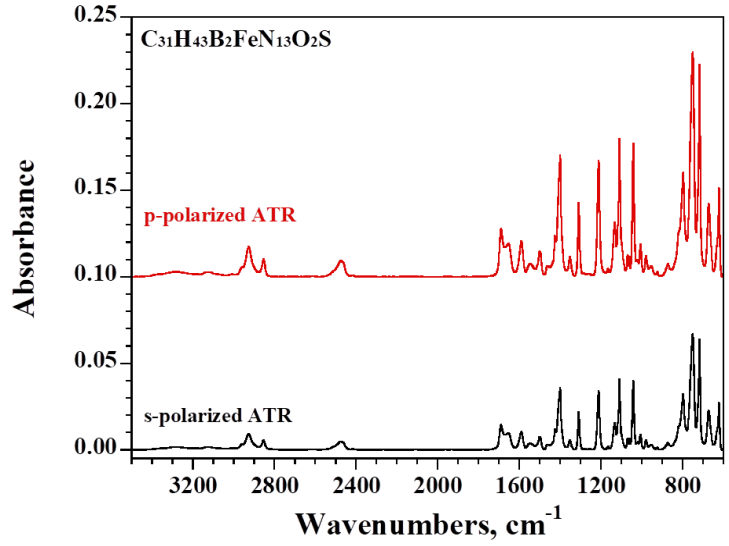

Figure S5b. Polarization-Modulated InfraRed Reflective Absorption Spectroscopy (PM-IRRAS)

P-polarized and s-polarized ATR spectra of **M**$_{SAc}$ film drop cast onto a Ge crystal.

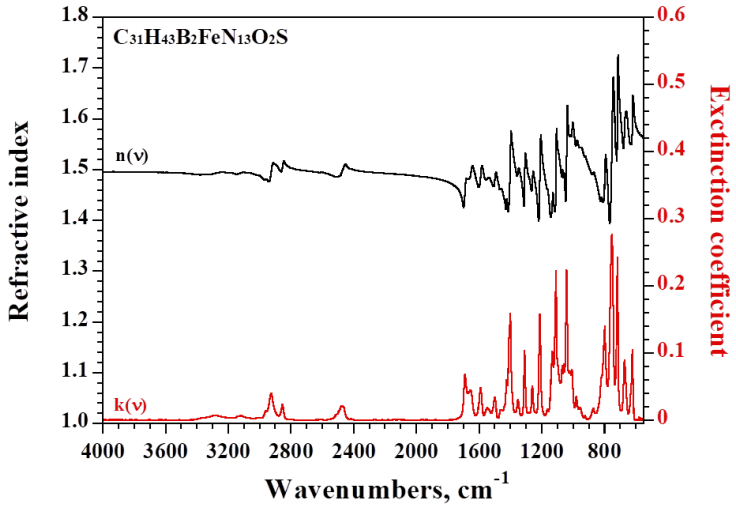

Figure S5c. Polarization-Modulated InfraRed Reflective Absorption Spectroscopy (PM-IRRAS)

Isotropic optical constants of **M**$_{SAc}$.

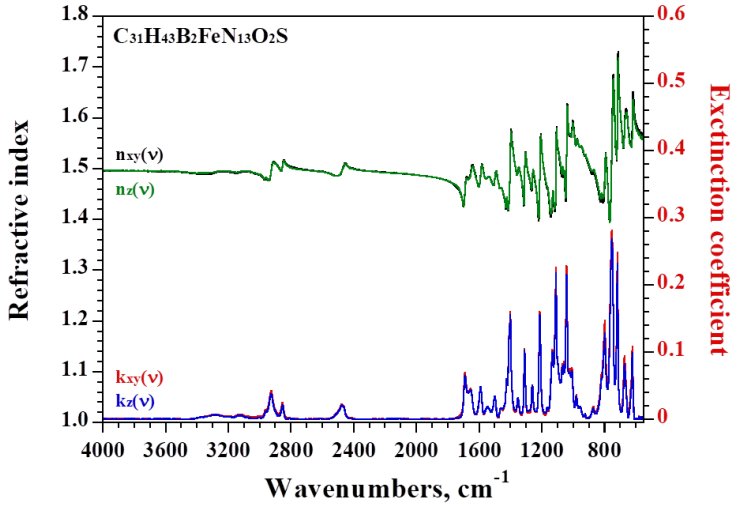

Figure S5d. Polarization-Modulated InfraRed Reflective Absorption Spectroscopy (PM-IRRAS)

Anisotropic optical constants of **M_{SAc}**.

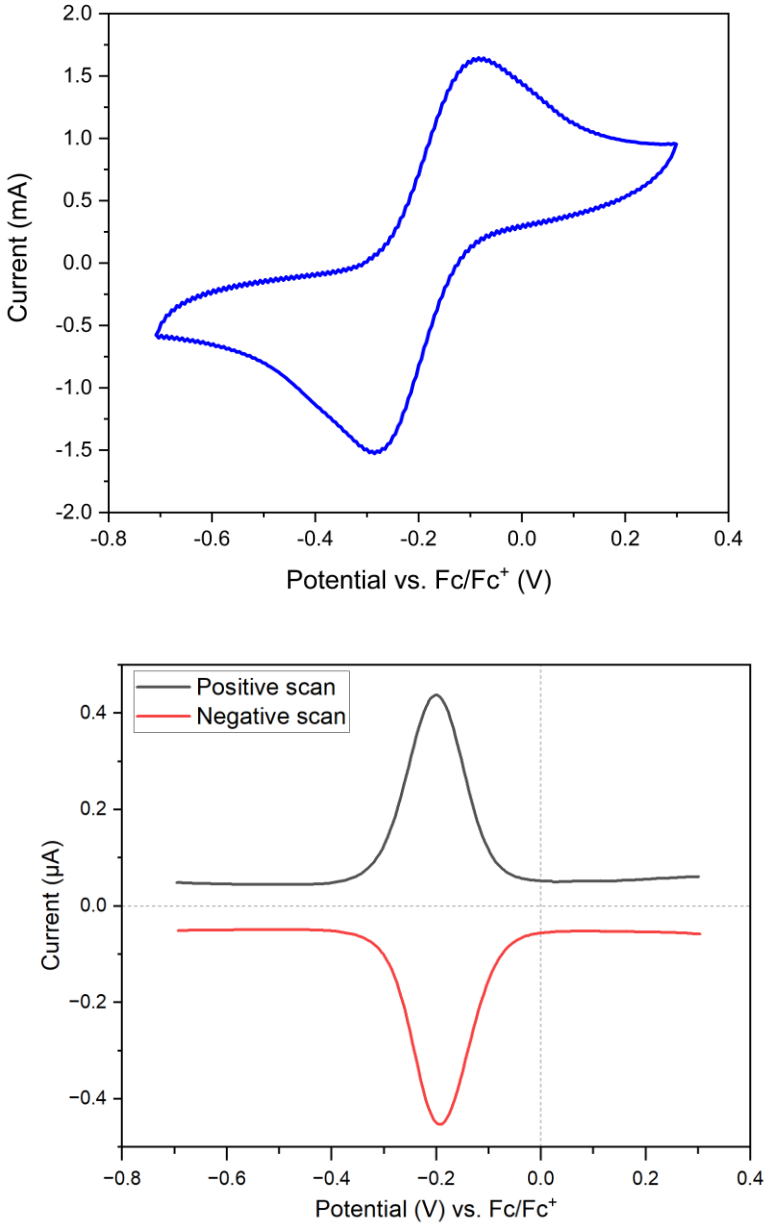

Figure S6. Electrochemistry

Cyclic voltammogram (top) and square wave voltammogram (bottom) of bulk **M**$_{\mathbf{SAc}}$ measured in a solution of THF with 0.1 M NBu_4PF_6 at a scan rate of 0.05 V s^{-1}. The half-cell potential is -0.18 V with respect to the ferrocene Fc/Fc^+ redox couple.

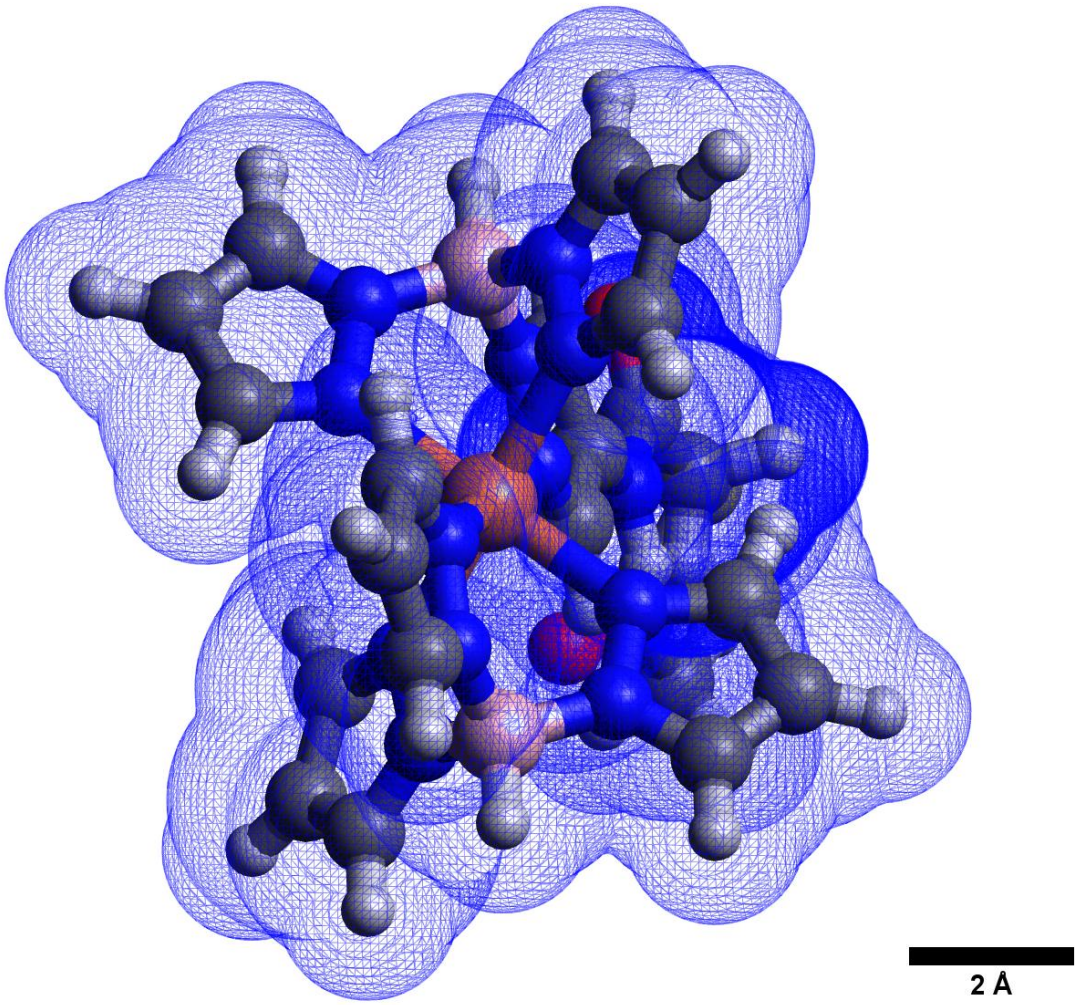

Figure S7. Geometry optimization

The geometry of **M$_{SH}$** as calculated by gas-phase DFT, from a point-of-view opposite to the thioalkyl chain. The cross section of the head group of the molecule is 0.91 nm^2.

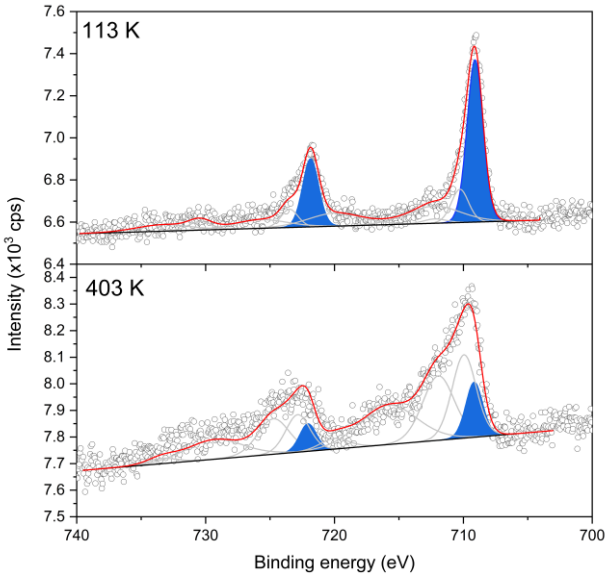

Figure S8a. Variable-temperature XPS

Variable temperature XPS in the Fe*2p* region on bulk **M$_{SAc}$**. As in the main text, the measured data is plotted as open circles, with the solid red lines corresponding to the envelopes of the fitted components, themselves shown as grey solid lines. The blue shaded regions are representative of the proportion of LS Fe(II) in the sample. As in the SAM, the combined area of these peaks clearly decreases with increasing temperature, consistent with the occurrence of thermal SCO in the sample. Besides being qualitatively similar, the bulk and SAM spectra also yield comparable relative areas for the blue shaded peaks at each temperature.

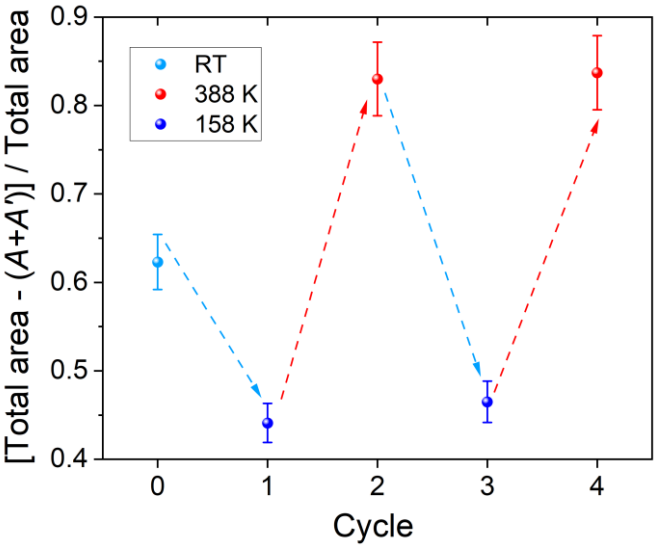

Figure S8b. Variable-temperature XPS

The approximated (the XPS is non-quantitative in this case) high spin fraction n_{HS} calculated from the relative (%) area of the shaded pair of peaks *A*+*A'* in **Figure 4**, indicative of LS Fe(II),

with cycling between 158 and 388 K. The areas do not change over the course of cycling, indicating that the SCO in the SAMs is reversible and that there is no sample degradation.

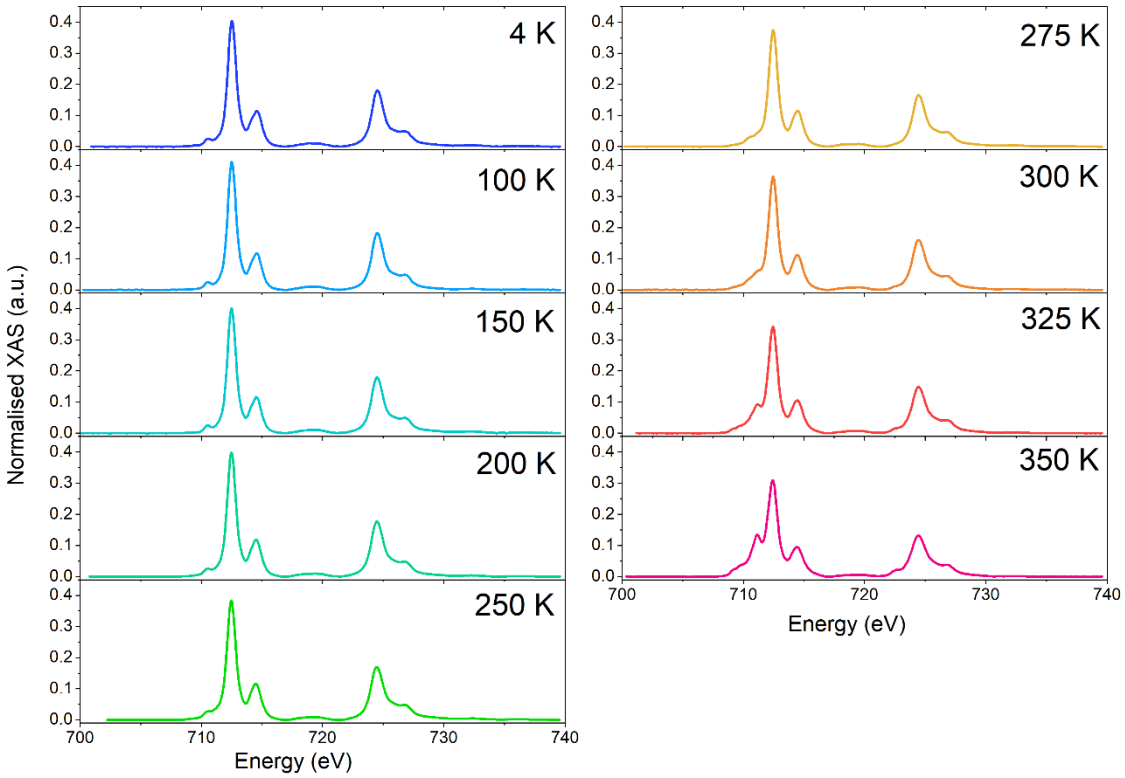

Figure S9a. X-ray Absorption Spectroscopy (XAS)

Evolution of the Fe $L_{2,3}$ edge XAS spectra with temperature on a dropcast sample of $\mathbf{M_{SAc}}$ on copper foil. Linear and step backgrounds have been subtracted and the spectra normalized to have the same total L_3 + L_2 area. The evolution of the spectra with temperature is comparable to that of the SAM spectra: the bulk and SAM exhibit a comparable SCO behavior.

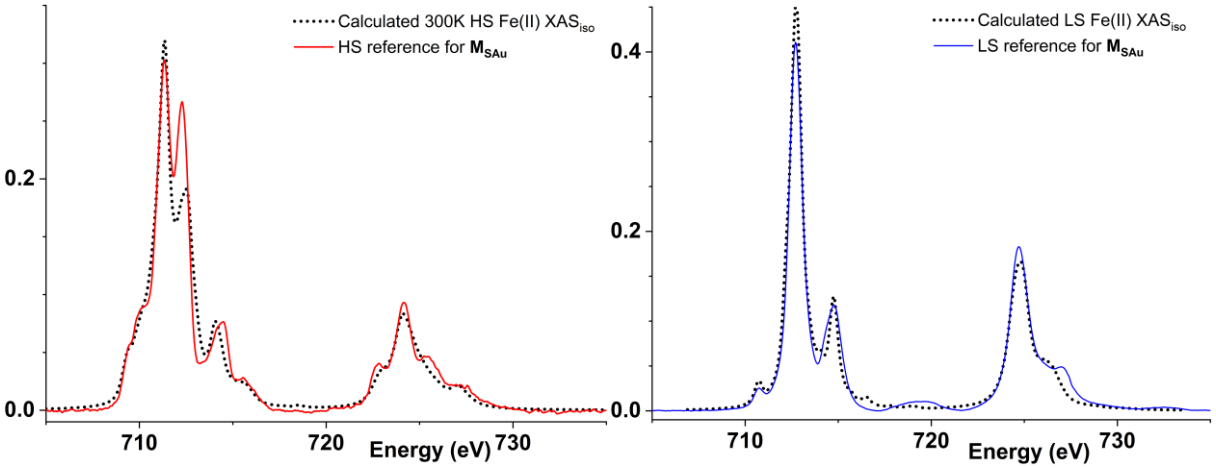

Figure S9b. X-ray Absorption Spectroscopy (XAS)

For the XAS reference spectra we used the dropcast spectra measured at 100 and 350 K after baseline correction and normalization. We assume that the spectrum at 100 K is fully LS, and subtract a fraction of this spectrum, after renormalization, from the spectrum at 350 K in order to obtain the HS reference.

These reference spectra are compared to those obtained through ligand field multiplet calculations (black dotted lines) for octahedral HS and LS Fe(II) (10*Dq* = 1 eV and 2.2 eV respectively) that we have previously reported.[7] The calculation energies were shifted by 1.2 and 1.9 eV to conform to experimental energies, and the spectra were normalized in the same way.

The discrepancies for the measured HS spectra are mainly at the L_3 edge 712.3 eV peak, likely because at 350 K there is not enough HS to allow for a perfect extraction of the HS spectral shape. For the LS spectra, deviations are seen for the feature between 717.0 and 721.0 eV, which is difficult to reproduce within the ligand field multiplet calculations as it likely originates from states delocalized over the ligand, and for the L_2 edge 727.2 eV peak. The relative variation of the L_3 and L_2 intensities due to the evolution of the branching ratio is in agreement between the experimental and calculated spectra.

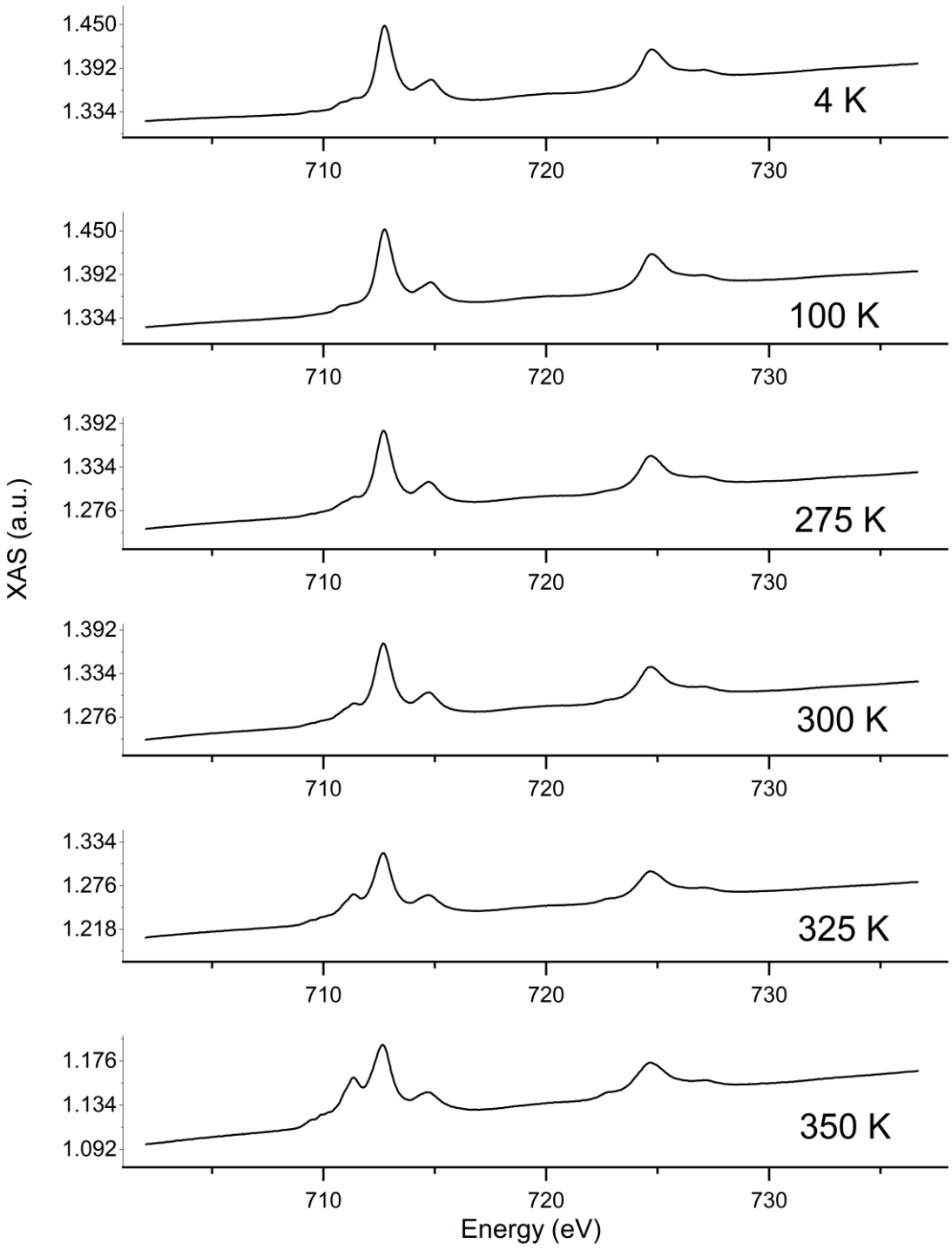

Figure S9c. X-ray Absorption Spectroscopy (XAS)

The raw, averaged spectra of an **M$_{SAu}$** SAM before the baseline corrections and normalization.

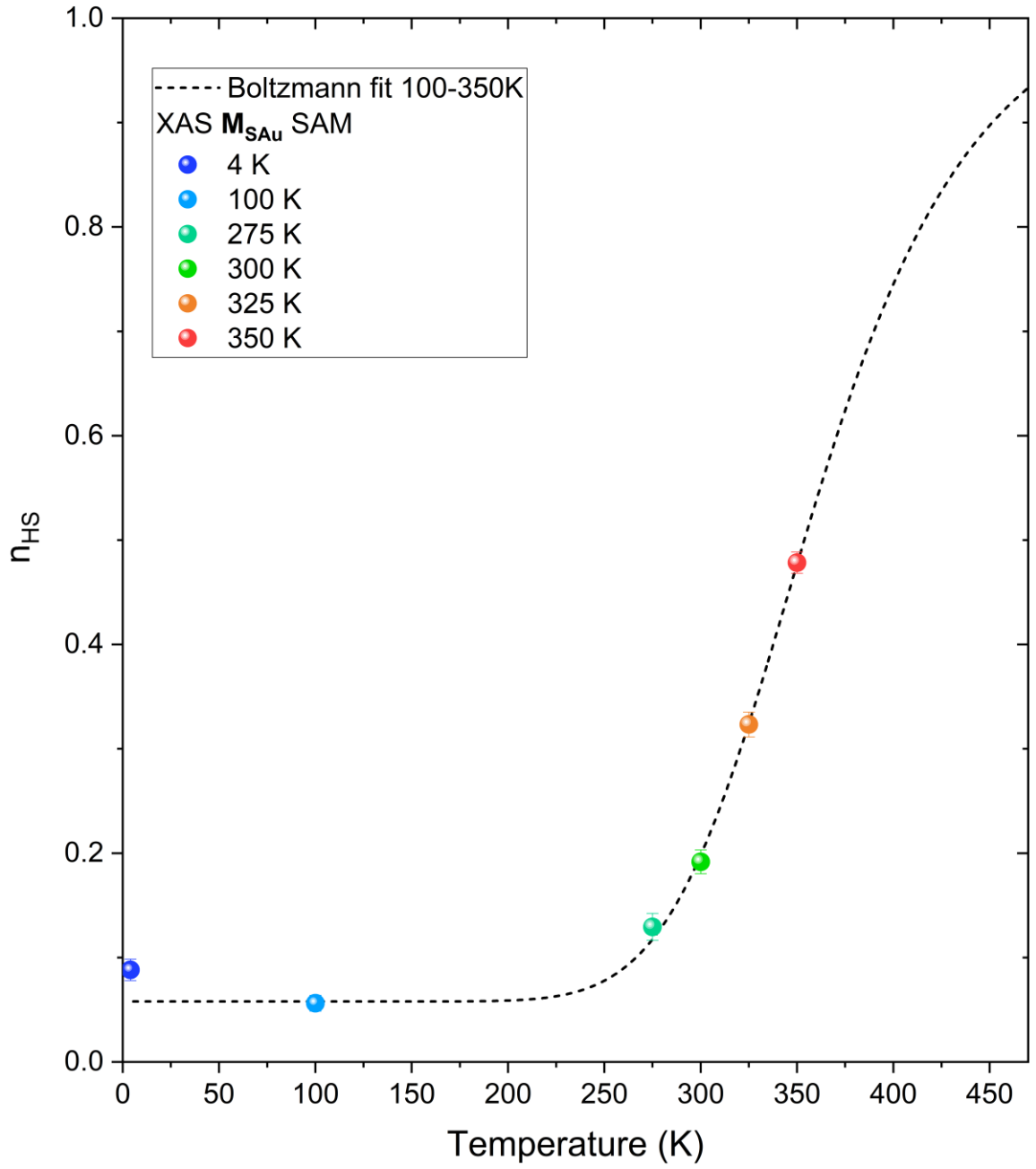

Figure S9d. X-ray Absorption Spectroscopy (XAS)

We fitted the XAS measurement considering the Boltzmann equilibrium between the two states described by Eq. 2:

$$n_{HS} = \frac{1}{1+exp(\Delta H/_{RT}+\Delta S/_{R})} + residue \qquad \text{Eq. 2}$$

We obtained a very satisfying fit (R^2 of 0.9999) with ΔH and ΔS values of 25.9(15) kJ mol^{-1} and 71(4) J K^{-1} mol^{-1} which are in very good agreement with the values calculated from the bulk magnetic data (Figure S1). We obtain here $T_{1/2} = \Delta H/\Delta S = 363$ K, a value. The residue of 0.058(6) is nevertheless superior to the 0.0189(2) calculated from the fit on bulk magnetometric values (Figure S1).

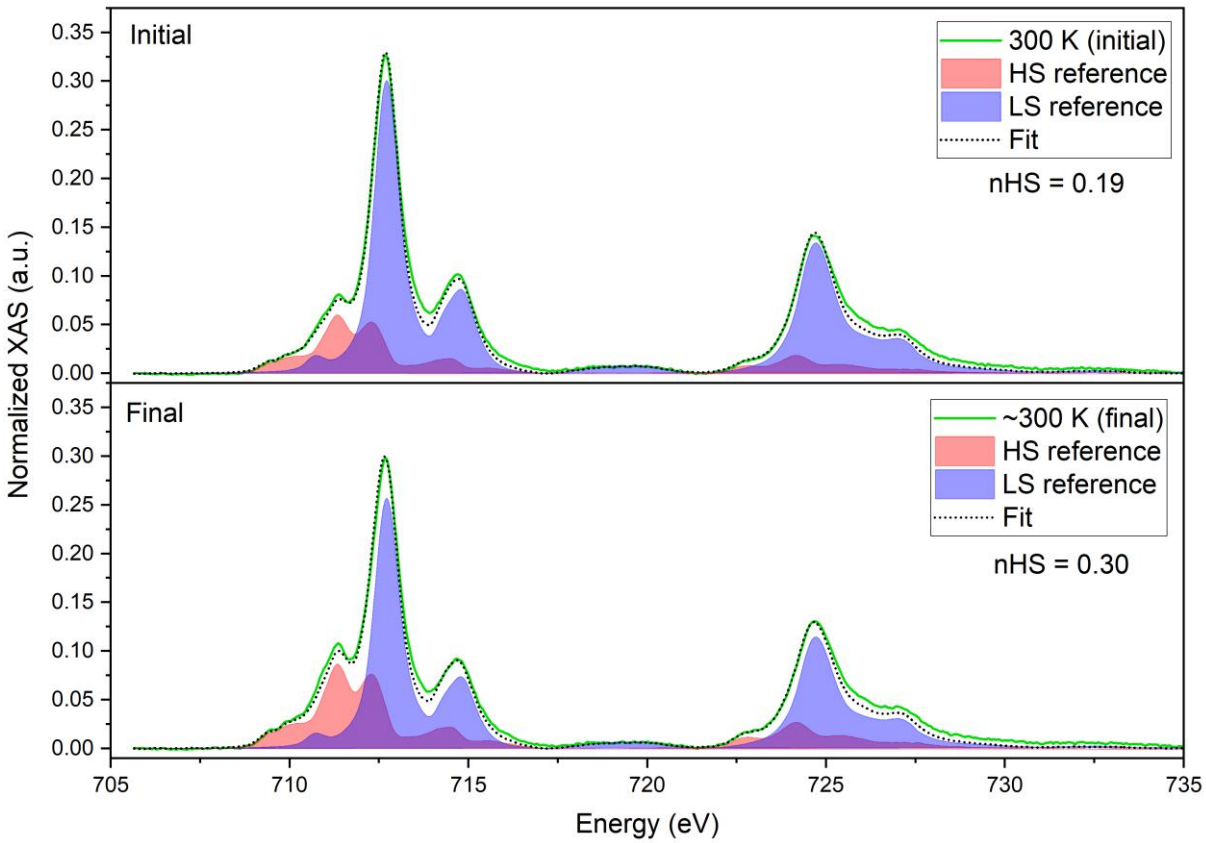

Figure S9e. X-ray Absorption Spectroscopy (XAS)

Variable temperature XAS on an $\mathbf{M}_{\mathbf{SAu}}$ SAM: the initial measurement at 300 K compared to the final measurement after the temperature sweep (300 K $\rightarrow$ 4 K $\rightarrow$ 350 K $\rightarrow$ 300 K). The experimental data (background corrected) is plotted in green, the linear regression as a dashed black line, and the relative components of LS and HS upon fitting the data are shown in blue and red, respectively. Note that the final measurement was performed when the sample was not fully cooled to 300 K, which could explain the difference in calculated n_{HS}.

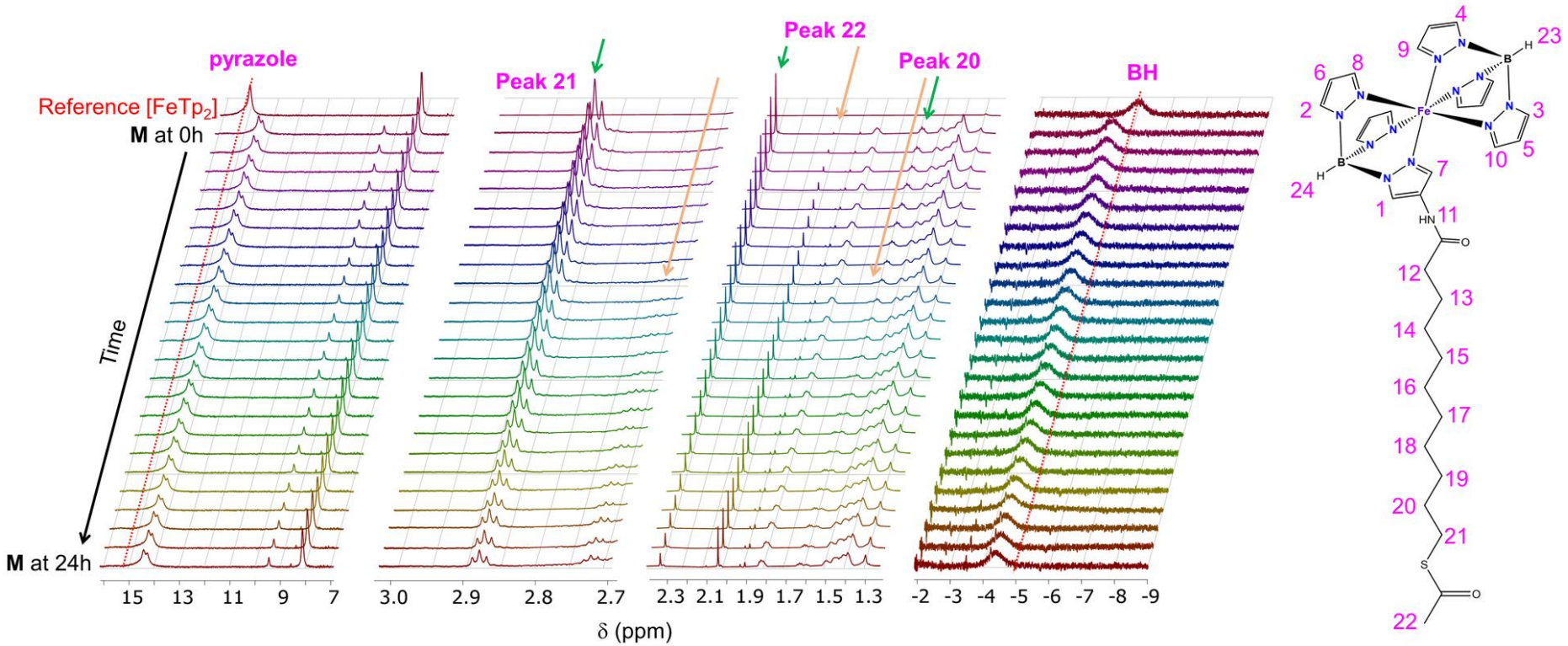

Figure S10. ^{1}H NMR monitoring of stability in solution

^{1}H-NMR spectra of an [FeTp$_2$] reference (top), and **M$_{SAc}$** over 24 hours (all other spectra), in 0.5 mL deuterated methanol solvent with 10 µL triethylamine, following the proton numbering for **M$_{SAc}$** used in the inset. The positions of the [FeTp$_2$] pyrazole and BH peaks are indicated by the red dashed lines. Neither appears in the spectrum of **M$_{SAc}$** over 24 hours, indicating that the molecule is stable and does not rearrange in solution to form [FeTp$_2$] and the bis-functionalized compound. The green and orange arrows indicate the peak positions before and after deprotection of the thioacetate, respectively.

References

[1] Yeh, J. J.; Lindau, I. Atomic Subshell Photoionization Cross Sections and Asymmetry Parameters: 1 - Z - 103., *At. Data Nucl. Data Tables* **1985**, 32, 1-155.

[2] Dignam, M. J.; Mamiche-Afara, S. Determination of the Spectra of the Optical Constants of Hulk Phases via Fourier Transform ATR. *Spectrochim. Acta* **1988**, 44A (12), 1435–1442. https://doi.org/10.1016/0584-8539(88)80195-8.

[3] Hansen, W. N. Electric Fields Produced by the Propagation of Plane Coherent Electromagnetic Radiation in a Stratified Medium. *J. Opt. Soc. Am.* **1968**, 58 (3), 380. https://doi.org/10.1364/JOSA.58.000380.

[4] Buffeteau, T.; Desbat, B. Thin-Film Optical Constants Determined from Infrared Reflectance and Transmittance Measurements. *Appl. Spectrosc.* **1989**, 43 (6), 1027–1032. https://doi.org/10.1366/0003702894203813.

[5] Yamamoto, K.; Ishida, H. Interpretation of Reflection and Transmission Spectra for Thin Films: Reflection. *Appl. Spectrosc.* **1994**, 48 (7), 775–787. https://doi.org/10.1366/0003702944029839.

[6] Palik, E. D. *Handbook of Optical Constants of Solids*; Academic Press: New York, U. S. A., **1985**.

[7] Warner, B.; Oberg, J. C.; Gill, T. G.; El Hallak, F.; Hirjibehedin, C. F.; Serri, M.; Heutz, S.; Arrio, M.-A.; Sainctavit, P.; Mannini, M.; Poneti, G.; Sessoli, R.; Rosa, P. Temperature- and Light-Induced Spin Crossover Observed by X-Ray Spectroscopy on Isolated Fe (II) Complexes on Gold. *J. Phys. Chem. Lett.* **2013**, 4 (9), 1546–1552. https://doi.org/10.1021/jz4005619.